CrossMark

Effects of annealing temperature and dopant concentration on the structure, optical, and magnetic properties of Cu-doped ZnO nanopowders

S. A. Ahmed[1,2]

Abstract This study analyzed the effects of annealing temperature and dopant concentration on the structural, optical, and magnetic properties of Cu-doped ZnO nanopowders. Cu-doped ZnO nanopowders were prepared using a solid-state reaction method. The X-ray diffraction results demonstrated that the Cu ions successfully substituted the Zn ions in the hexagonal wurtzite structure of the ZnO nanoparticles. Ultraviolet–visible spectroscopy measurements revealed that the band gap decreased due to the incorporation of Cu. The photoluminescence results showed that the intensity of the emissions increased with doping and decreased as the annealing temperature (T_A) increased, which can be attributed to the increase and decrease of the oxygen vacancies (V_O), respectively. The magnetic properties of the ZnO nanopowders were also found to be affected by Cu doping and T_A. The ferromagnetic behavior of the ZnO nanopowders decreased as both the doping concentration and T_A increased. This behavior can be explained by the increase in the antiferromagnetic superexchange interaction along with Cu doping due to the decrease in the distance between the Cu ions and the decrease in V_O, respectively. Thus, the results indicate oxygen stoichiometry and V_O both play a dominate role in the room temperature ferromagnetic response of ZnO nanopowders.

✉ S. A. Ahmed
saadzf2003@gmail.com

1   Physics Department, Faculty of Science, Sohag University, Sohâg 82524, Egypt

2   Physics Department, College of Arts and Science, Qassim University, P.O. 3137, Unayzah 51911, Saudi Arabia

1 Introduction

Currently, there is a lot of interest in the science and potential technological applications of spin transport electronics, or spintronics, in which the spin of charge carriers is exploited to provide new functionality for electronic devices [1]. To develop multifunctional devices, it is essential to combine the charge and spin of the electrons that can be used as an added degree of freedom in new electronic devices [2]. Spintronics, a new area in the field of science, explores the physics of previously unavailable combinations of electronic, optical and magnetic properties in semiconductors. Diluted magnetic semiconductors (DMSs) represent a synergetic collaboration between charge-based semiconductors and spin-based magnetism [1]. DMSs, which are emerging as promising spin injection sources, are a prerequisite for advancing the field of spintronics, and their possible functionalities have recently attracted broad interest. The discovery of many DMS materials with room-temperature ferromagnetism (RTFM) has generated a lot of interest because of their scientific and technological importance. Theoretical studies have predicted, and experiments have verified that some wide-band-gap oxide semiconductors (such as ZnO, TiO_2, GaN, etc.) doped with transitional metals (e.g., Mn, Fe, Co, Ni, V, Cr and Cu), are DMSs [3–5]. However, the consensus is that the experimental results on oxide-based DMSs are difficult to interpret owing to the low doping concentration and the reduced conductivity, both disfavoring carrier-based mechanisms [6]. Furthermore, in spite of the growing interest in DMSs, there is no explicit agreement about the nature and origin of the observed ferromagnetism (FM) in the diluted magnetic oxide that is doped with a few percent of 3d cations. The scientific community is still debating about whether FM is indeed intrinsic, that is, mediated by

carriers or defects inside the host semiconductor, or if it is purely extrinsic, due to the formation of ferromagnetic secondary phases, metallic clusters or impurities [7, 8].

In this context, the scientific community has responded enthusiastically to recent reports about the observation of RTFM in ZnO:Cu. This is mostly because neither copper (Cu) nor its oxides (CuO and Cu_2O) are ferromagnetic [9]. Therefore, ZnO:Cu has the possibility of being free of ferromagnetic impurities; hence, it could form an intrinsic DMS. Thus, if any FM is observed in a Cu-based system, it will undoubtedly be the inherent property of the material. Nevertheless, the ZnO:Cu system is controversial. A recent magnetic circular dichroism study of ZnO:Cu thin films did not detect any significant spin polarization on the Cu 3d and O2p states, although the samples showed RTFM, and they were free of contamination [7]. Such intriguing results suggest that the origin of RTFM in ZnO:Cu is different from the carrier-mediated mechanism, and this warrants further investigation.

To date, recent investigations of ZnO:Cu DMS have primarily focused on the films [8, 10–12]. A survey of the literature shows that few studies have examined RTFM in ZnO:Cu nanostructures, and a comprehensive study of the structural, optical characteristics, and magnetic properties of ZnO:Cu nanopowders has not yet been conducted. More studies have shown that the annealing temperature (T_A) plays an important role in microstructures and the optical and magnetic properties of magnetic materials [8, 10, 12–15]. Therefore, the present investigation provides details on the effects of dopant concentrations and T_A on the structure, optical characteristics, and magnetic properties of $Cu_xZn_{1-x}O$ ($2 \leq x \leq 0.06$) nanopowders that are synthesized using a solid-state method.

2 Experimental details

2.1 Preparation of the samples

Nanopowder samples of nominal compositions of $Cu_xZn_{1-x}O$ (x = 0.02, 0.04 and 0.06, hereafter referred to as ZC2, ZC4, and ZC6, respectively.) were synthesized via a standard solid state reaction route. In this route, appropriate amounts of ZnO (99.9% purity, Sigma-Aldrich) and Cu_2O (99.9% purity, Strem Chemicals Inc.) were ground for 3 h to obtain homogeneous mixtures according to the required compositions. The resulting powder underwent calcination at 400 °C for 8 h in air, followed by furnace cooling up to room temperature (RT). The resulting material was reground and pressed into dense pellets before being sintered at 500 °C in air for 12 h, followed by furnace cooling. Additionally, two different parts of 2% Cu-doping nanopowders (pre-heated at 400 °C for 8 h in air) were

annealed at various temperatures of 600 and 700 °C (the ZC2-600 and ZC2-700 samples). Finally, the pellets were ground for 3 h to obtain the homogeneous $Cu_xZn_{1-x}O$ ($2 \leq x \leq 0.06$) nanopowder samples.

2.2 Characterization techniques

To characterize the structure of the prepared samples, X-ray diffraction (XRD) measurements were taken using a PANalytical X'Pert PRO diffraction system with 1.54 Å of CuK_α radiation. The optical properties of the samples were characterized using ultraviolet–visible spectroscopy (UV–Vis) (CARY 5000) with a wavelength of 200–800 nm and photoluminescence (PL) spectrophotometer (CARY Eclipse, $\lambda = 381$ nm) in the range of 400–800 nm. The magnetic properties (M(H) loops) of the samples were measured using a Lakeshore vibrating sample magnetometer (VSM) (Model no. 7410).

3 Results and discussion

3.1 X-ray diffraction (XRD)

Figure 1 shows the XRD patterns of the ZnO:Cu samples: (a) undoped ZnO, (b) ZC2, (c) ZC4, (d) ZC6, (e) ZC2-600, and (f) ZC2-700, respectively. The XRD analysis showed that all the samples had a polycrystalline hexagonal wurtzite structure. The pattern can be indexed for diffractions from the (100), (002), (101), (102), (110), (103), (200), (112), (201), (004), and (202) planes of the wurtzite crystals corresponding to ZnO. The XRD also showed some weak diffraction peaks attributed to CuO [16] (Fig. 1). This result is consistent with the low solubility limit ($\sim$1%) of Cu in ZnO [17]. This present study found that, as the Cu content increased, the CuO diffraction peaks became evident and stronger. Moreover, by increasing T_A from 500 to 700 °C, the CuO diffraction peak increased (ZC-600) and decreased (ZC-700), respectively. When copper ions were
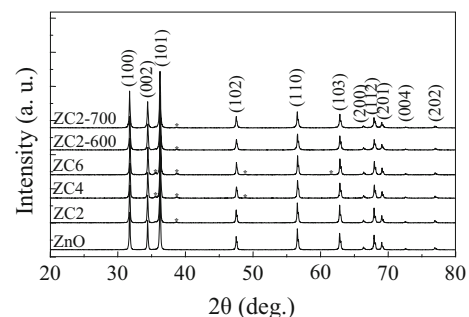
Fig. 1 RT θ–2θ XRD spectra of ZC2, ZC4, ZC6, ZC2-600, and ZC2-700 samples. Peaks are indexed to the hexagonal wurtzite structure, while CuO peaks, when present, are marked by the *asterisk*

introduced as dopants, the width broadened as a result of the increase in disorder on Cu^{2+} [18, 19]. The diffraction intensities were weaker in the doped sample than the undoped ZnO, which illustrates that Cu doping can slightly impede the crystallinity of ZnO.

The average particle size for the undoped ZnO was estimated to be about 27.5 nm from the X-ray line broadening using the Scherrer formula $D_{hkl} = K\lambda/\beta_{hkl}Cos\theta$, where D_{hkl} is the particle diameter, K is the Scherer coefficient (K = 0.89), β is the full width at half maximum (FWHM), and λ is the wavelength of X-rays. Slightly more broadening of the peaks was observed in the Cu-doped samples, and this is understood to be due to the additional thermodynamic barrier to the nanocrystals' growth as a result of the added dopant [18]. The average particle size of the ZnO:Cu nanopowders was found to be 26.3–24.9 nm (Table 1). The reduction in the crystal size is mainly due to the distortion in the host ZnO lattice caused by the foreign impurity, i.e. Cu^{2+}, which also decreases the nucleation and subsequent growth rate by the addition of different Cu concentrations [18–20]. The average particle size calculations for the Zn:0.02CuO nanopowders annealed at 500 °C (ZC2), 600 °C (ZC2-600), and 700 °C (ZC2-700) indicate a minuscule improvement from 26.3 to 26.7 nm when T_A increased from 500 to 700 °C; this implies that only limited sintering occurs. This means that the random distribution of nanograins critically influences the microstructural properties of the materials by changing the local disorder and surface defects. Furthermore, the marginal improvement in the particle size, on the one hand, could be due to the existence of the CuO secondary phase in the sample, which prevents grain growth, and on the other hand, the inhibit in the oxygen vacancy (V_O) concentration due to annealing at high temperatures (i.e. 600 and 700 °C), which also inhibits growth, as reported by Zhang et al. [21]. Moreover, since the surface-to-volume ratio is very high in the nanocrystalline phase, surface defects play an important role. These defects have some impact on grain size development with annealing, as grain growth is restrained by the nanoscale grain size that has more defects on the surface and by the grain boundary [22]. However, these findings are compatible with the PL results (discussed below in Sect. 3.3).

A shift in the XRD peak positions related to the changes in the lattice parameter was also clearly observed when the Cu concentration and T_A varied. The diffraction peaks of the ZC2 sample shifted to the lower angle, and the lattice parameters increased (a = 3.2531 Å; c = 5.2125 Å) in comparison to ZnO (a = 3.2495 Å; c = 5.2065 Å), as shown in Table 1. The calculated lattice parameters were also in agreement with the reported values [19]. Since the radii of the octahedral coordinated Cu^{2+} ions (0.057 nm) are slightly smaller than those of the Zn^{2+} ions (effective ionic radius of 0.060 nm), substitutional doping of Cu into the ZnO lattice should cause the diffraction peak to shift to a higher angle. The lower angle shift is possible due to the non-uniform substitution of the Cu ion into the ZnO site [23, 24]. This increment could also be due V_O formation in the nanopowders, as reported by Sundaresan et al. [25]. Because the ZnO is an ionic crystal, the formation of V_O induces a profound structural relaxation as a consequence of the repulsion of the nearby Zn ions [15]. From the tabulated data, shifts toward lower values of the lattice parameters due to increases in the dopant concentration (x > 2%) and T_A, were also observed for most of the samples; however the 'a' constant for the ZC2-700 sample increased. Defects and imperfections in the grain of the ZC2-500 sample exert higher compression stress on the lattice, resulting in larger lattice parameters. The shifting and broadening of the XRD lines, with both doping and annealing, strongly suggest that Cu^{2+} has successfully been substituted into the ZnO host structure at the Zn^{2+}; which is similar to the findings from previous studies [19, 20, 23, 24].

3.2 UV–Visible absorption and energy gap calculation

UV–visible absorption spectroscopy (UV–Vis) is a powerful technique that is used to explore the optical properties of semiconducting nanopowders. Fig. 2 shows the UV–Vis optical absorption spectra and clear pictures of the

Table 1 Lattice and magnetization parameters, and grain size for ZC2, ZC4, ZC6, ZC2-600, and ZC2-700 samples

Samples	Lattice		Grain size (nm)	M_s	M_r	H_c (G)	M_s
	Parameter (Å)	Volume (Å³)		10^{-3} emu/g			10^{-3} μB/Cu
ZC2	a = 3.2531; c = 5.2125	47.76	26.27	27.70	0.41	205	36
ZC4	a = 3.2526; c = 5.2082	47.70	25.28	24.68	0.33	163	16
ZC6	a = 3.2521; c = 5.2060	47.67	24.90	23.43	0.28	145	10
ZC2-600	a = 3.2509; c = 5.2122	47.69	26.57	22.86	0.30	193	29
ZC2-700	a = 3.2541; c = 5.2087	47.75	26.65	21.42	0.26	184	27

absorption changes in the $Cu_xZn_{1-x}O$ nanopowders. The absorption spectra indicate that the absorption initially increases from x = 0 to 0.04, then it decreases with the additional Cu doping (x = 0.06; ZC6); the sample where x = 0.04 (ZC4) has a higher absorption than the other samples. The absorption edge exhibits a blue shift after x = 0.02, whereas it exhibits a red shift from x = 0 to 0.02. Furthermore, with the increase in T_A from 500 to 700 °C, the absorption edge exhibits a red shift. This can be attributed to the decrease in V_O or the surface defects due to annealing at high temperatures. The calculated band gap for the ZC2, ZC4, ZC6, ZC2-600, and ZC2-700 nanopowders are: 3.187, 3.204, 3.196, 3.077, and 2.109 eV, respectively. The optical band gap (E_g) of the samples was determined by using the formula, $E_g = hc/\lambda$, where h is plank's constant, c is the velocity of light, and λ is wavelength [18]. The E_g values are similar to those reported for Cu-doped ZnO nanorods [19] and nanocrystals [26]. The E_g values for x = 0.02 (ZC2), 0.04 (ZC4), and 0.06 (ZC6) were found to increase with the growth of Cu doping [18, 27], which may be explained by the Burstein–Moss shift. In comparison to the undoped ZnO nanopowders ($\sim$3.22 eV), the E_g value for the ZC2 nanopowders is lower [19, 26, 28, 29]. A similar narrowing of E_g was also observed with increasing T_A. It is interesting to note that as T_A increased, the E_g values decreased [13, 30], indicating an apparent red shift, which may be attributed to the rigid shift in the valence and the conduction bands due to the coupling of the band electrons and the localized Cu^{2+} impurity spin [16]. Therefore, it has been concluded that the nanometric size of the grains and their distributions significantly influence the local electronic structure of the Cu-doped ZnO lattice.

3.3 Photoluminescence

Photoluminescence (PL) is a useful technique used to determine defects in wide band gap oxides. To reveal the effect of Cu doping and T_A on the PL properties of the ZnO nanopowders, PL was measured at RT. Figure 3 shows the
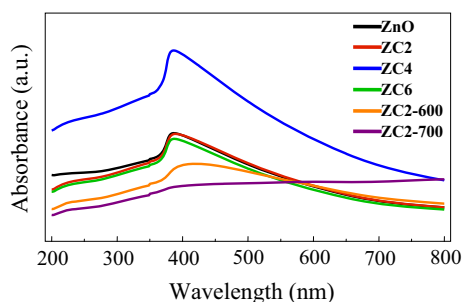
PL spectra of the ZC2, ZC4, ZC6, ZC2-600, and ZC2-700 nanopowders by exciting the sample at 381 nm. The shape of the PL spectra for the ZnO nanopowders is similar to those reported by others [31, 32]. As seen in Fig. 3, the samples have three emission bands: (i) a predominant peak at 424 nm corresponding to the violet region, (ii) low-intensity peaks centered at 448 and 461 nm, representing the blue region, and (iii) strong peaks centered at 486 and 521 nm, representing the green band. The defect levels created by Cu do not appear to form a luminescence center because the PL emission band matches that of the undoped ZnO [18, 19, 26]. It has also been observed that the position of different emission peaks is nearly constant for all the samples [26]. It is the intensity of the emission peaks that changes with Cu doping and T_A. Compared with the undoped ZnO sample, the intensity of the PL emissions increased after Cu was introduced into the sample [18]. This indicates that Cu doping increases the radiative recombination processes. The intensity of the Cu^{2+} emission increases at 2–4%, and then it decreases again at 6%. The reduction in the emission intensity at 6% can be explained by the concentration quenching effect [10]. The intensity of the PL emissions of the ZC2 sample also decreased slightly as the T_A increased from 500 to 600 °C (ZC2-600), and then it was reduced significantly as the T_A further increased to 700 °C (ZC2-700). However, in the ZC2-700 sample, the green peak located at about 521 nm showed that the intensity is only slightly increased (by a factor of $\sim$2%), becoming nearly identical to the intensity of the ZC2 sample that was annealed at 500 °C. This behavior may be due to the reduction in the concentration of V_O with increasing T_A from 500 to 700 °C, which, in turn, decreased the concentration of the recombination centers. It was concluded that the ZC2 sample annealed at 500 °C had higher PL emissions than the ZC2-600 and ZC2-700 samples annealed at higher temperatures of 600 and 700 °C, respectively, due to the higher V_O concentration in the sample annealed at a lower temperature (ZC2; 500 °C). Based on these arguments, the high V_O concentration may be responsible for the higher intensity of the PL

Fig. 2 (Color online) RT UV–Vis absorption spectra of ZC2, ZC4, ZC6, ZC2-600, and ZC2-700 samples
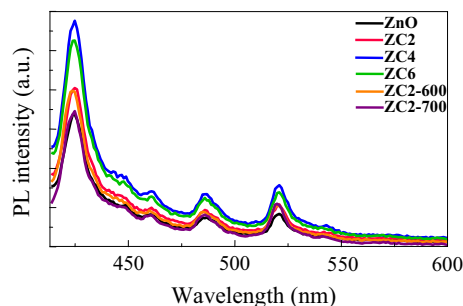
Fig. 3 (Color online) RT PL spectra of ZC2, ZC4, ZC6, ZC2-600, and ZC2-700 samples

emissions of the sample that was annealed at a low temperature (ZC2; 500 °C).

Interestingly, the origin of the PL emissions is questionable because these emissions have been observed in both the undoped and ZnO:Cu samples. Previous experimental and theoretical results have shown that V_O originates in the violet luminescence [33–37] and blue luminescence in ZnO [35, 38–41], which is consistent with the results observed in this present study. A higher intensity of the violet luminescence may be attributed to more grain boundary defects in the sample, while a low blue emission could be because the neutral oxygen vacancy (V_O^x) centers are not underactive ionized, which is a response to the absence of a blue emission in bulk ZnO [40]. As for the green luminescence in ZnO, it is accepted that this is due to the singly ionized oxygen vacancy (V_O^+) [38, 41–44]. The V_O^+ charged center can easily trap a photoexcited electron through a non-recombination step to form V_O^x, which is unstable at RT. Then, a radiative recombination of the V_O^x charged center with the photoexcited holes in the valance band effectively occurs, giving rise to green emissions, which were also observed in this present study [38, 42]. However, zinc vacancies and oxygen interstitial defects often have higher formation energy than V_O, and these can only form in oxygen-rich environments [45]. Due to the lower formation energy of V_O in oxides compared with cation interstitials [46], the oxygen deficiency in ZnO is attributed to V_O instead of the zinc interstitials. Besides, according to an earlier report [47], the zinc interstitial is not a stable defect in ZnO at RT. Mishra et al. [48] also reported that the Zn_i defects are highly mobile at and above 400 °C, and they are likely to recombine with the V_{Zn} that is dominant in ZnO nanocrystal grain boundaries. Furthermore, Sanyal et al. [49] and Dutta et al. [50] showed that a significant number of V_O were produced and Zn_i atoms acquired sufficient energy and returned to the crystal lattice site (i.e., Zn_i recombined with V_{Zn}) by annealing the polycrystalline ZnO in the air at about 500 °C. Recently, Liu et al. [51] also demonstrated that when annealing ZnO:Co films in the air at 600 °C, the Zn_i atoms are returned to the crystal lattice site. Note that all of the samples in our case were annealed in ambient air, resulting in an oxygen-deficient ZnO crystal; consequently, the visible emission is most likely connected to the V_O defects. Thus, it is safe to conclude that V_O is the origin of the PL luminescences.

3.4 Magnetic measurements of the samples

The magnetic measurements of the samples using vibrating sample magnetometer (VSM) are shown in Fig. 4. The inset in this figure shows the magnification portion of the plot near
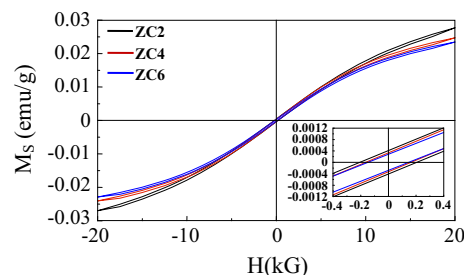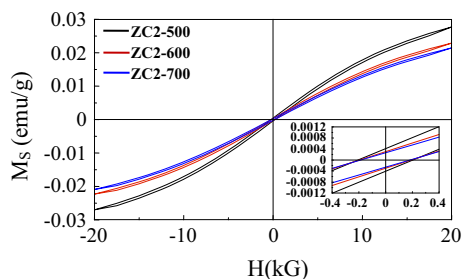

Fig. 4 (Color online) RT *M-H* curves of ZC2, ZC4, and ZC6 samples. The *inset* shows the RT hysteresis in the low-field region

the origin. Small but distinct evidence of ferromagnetic ordering was observed in all the samples. As Fig. 4 shows, after subtracting the diamagnetic background of the sample holder, all the samples demonstrate FM at RT. The parameters obtained from the M (H) data at 300 K are listed in Table 1. As seen in Table 1, the ZnO:0.02Cu sample (ZC2) shows RTFM with a saturated magnetic moment (Ms) of 27.70×10^{-3} emu g^{-1} (or Ms = 36×10^{-3} μ_B Cu^{-1}, based on the overall Cu concentration, which was almost three orders of magnitude larger than that of the undoped ZnO sample (not shown here), and a coercivity (Hc) of about 205 G (inset in Fig. 4). As the mass fraction of Cu increases, Ms changes to 24.68 emu g^{-1} (16×10^{-3} μ_B Cu^{-1}) and 23.43 emu g^{-1} (10×10^{-3} μ_B Cu^{-1}) for 4 and 6% Cu-doped ZnO (ZC4 and ZC6), respectively, suggesting that increasing the Cu-doping leads to a decrease in FM. Hc also decreases with doping: 163 and 145 G for 4% Cu and 6% Cu, respectively (Table 1). These Hc and Ms values agree closely with the results reported in other studies [11, 20, 23, 24, 26].

The ferromagnetic behavior shown in Fig. 4 is a compensation effect between the ferromagnetic system and the antiferromagnetic (AFM) superexchange interaction. The drop in moment per Cu atom with doping could be due to the increasing occurrence of AFM coupling between the Cu pairs occurring at shorter separation distances. The AFM was found to be present even at a low loading level (2%), and it continues to increase as the amount of transition metal increases. This implies that the AFM interaction becomes stronger with x, most likely due to the decreasing distance between the Cu ions [9–11, 18, 23]. Since the Cu atoms are separated, yet still closely situated near one another in the thin surface layers, the short-range Cu–O–Cu AFM superexchange should become more stable. Theoretical modeling of the $Cu_xZn_{1-x}O$ system indicates that where the Cu atoms are located in relation to concerning each other can strongly affect the magnetic properties of the system [17, 52]. From their ab initio study, Weissmann et al. [53] concluded that Cu impurities only produced a magnetic moment for very small concentrations, and they proposed that this depends strongly on the

distance between the Cu atoms. Besides, it is known that the CuO secondary phase is AFM material [54], and it could not contribute to the RTFM observed in the samples. The existence of the CuO secondary phase in the sample decreases the ferromagnetic ordering [16, 20, 23]. Furthermore, the formation of the CuO secondary phase most probably occurs at the surface, and it is accompanied by a reduction of Cu^{2+} [14]. It is well known that Cu ions may exist in Cu^+ or/and Cu^{2+} states. The 3d orbitals in Cu^{1+} are fully filled; hence they do not contribute to FM. The origin of the RTFM should be due to the Cu^{2+} ions. Accordingly, the magnetic moment per Cu atom should be reduced with the decrease in the concentration of Cu^{2+}, as observed in the present study.

In fact, the contribution of point defects, such as V_O, to the FM of transition metal doped ZnO samples has been reported by many research groups. To see how the total magnetization scales with T_A, two additional samples with 2% Cu annealed at different temperatures of 600 and 700 °C (ZC2-600 and ZC2-700) were investigated. Annealing in air eliminates the V_O of the samples. The total magnetization decreased as the T_A increased (Fig. 5). We also observed that the FM of the ZnO:0.02 CuO nanopowders decreased after annealing at higher temperatures. This present study's results prove that the RTFM of the ZnO:Cu nanopowders originates from V_O. The Ms was found to be 22.86 emu g^{-1} (29×10^{-3} μ_B Cu^{-1}) and 21.42 emu g^{-1} (27×10^{-3} μ_B Cu^{-1}), respectively, and Hc was found to be 193 and 184 G when annealing occurred at 600 and 700 °C (ZC2-600 and ZC2-700), respectively. The reduction in the magnetic moment for T_A above 500 °C may be attributed to the decrease in V_O, which degraded the magnetic exchange. Annealing can regulate the concentration of V_O at high air temperatures (600 and 700 °C). Thus, the Cu-doped ZnO system became less ferromagnetic when annealed at air temperatures of 600 and 700 °C. It is well-known that V_O and the densities of the defects have a significant effect on the physical properties of oxide nanostructures. This also suggests that defects play an essential role in the magnetic ordering in

ZnO:Cu materials. The PL study verified the correlation between structure and property.

From the above discussion and analysis, it can be seen that both the incorporation of donor defects and the substitution of Cu^{2+} for Zn in ZnO are assumed to be two key factors in introducing magnetic ordering in the ZnO:Cu samples. All the samples showed RTFM, but with a lower magnetic moment as both the mass fraction of Cu and T_A increased. Therefore, the RTFM is unlikely to be ascribed to secondary phases. The decrease in FM with increasing Cu concentration and T_A demonstrates that FM observed at RT is an intrinsic property of $Cu_xZn_{1-x}O$ nanopowders. Therefore, we suggest that the observed FM is intrinsic in all the samples [19]. The origin of the FM in ZnO:Cu nanopowders can be explained by a non-carrier mediated bound magnetic polarons (BMPs) model [55], which implies that ferromagnetic coupling between two Cu^{2+} ions is facilitated through V_O. Sufficient concentration of V_O defects, which exceed the percolation threshold, leads to V_O overlapping with the dopant ions, thereby forming BMPs [44, 56]. As the V_O density decreases with elevated temperatures, the number of BMPs decreases, which leads to the reduction of FM [12]. Therefore, it can be proposed that a V_O defect-mediated mechanism, such as a BMP-mediated mechanism, is responsible for FM in Cu-doped ZnO-based DMSs [8].

4 Conclusions

In summary, ZnO:Cu nanoparticles were successfully synthesized by a solid-state reaction route. The XRD results demonstrated that Cu ions were successfully substituted for Zn ions in the hexagonal wurtzite structure of the ZnO nanopowders. The UV–Vis measurements revealed that E_g decreased due to the incorporation of Cu, and it also decreased with increasing T_A. The PL intensity emissions were found to increase due to these substitutions, but they decreased with the increase in T_A due to the reduction in the V_O. The RT VSM study demonstrated that the Ms and Hc of the samples decreased with Cu doping and T_A because of the increase in the AFM superexchange interaction along with Cu doping, due to the decreasing distance between the Cu ions, and the decrease in V_O, respectively. Finally, it can be concluded that defects play an important role in manipulating the ferromagnetic and PL properties of ZnO nanopowders.

Fig. 5 (Color online) RT *M-H* curves of ZC2-500, ZC2-600, and ZC2-700 samples. The *inset* shows the RT hysteresis in the low-field region

References

1. H. Ohno, Science **281**, 951 (1998)
2. S.A. Wolf, D.D. Awschalom, R.A. Buhrman, J.M. Daughton, S. von Molnár, M.L. Roukes, A.Y. Chtchlkanova, D.M. Treger, Science **294**, 1488 (2001)

3. T. Dietl, H. Ohno, F. Matsukura, J. Cibert, D. Ferrand, Science **287**, 1019 (2000)
4. Y. Matsumoto, M. Murakami, T. Shono, T. Hasegawa, T. Fukumura, M. Kawasaki, P. Ahmet, T. Chikyow, S. Koshihara, H. Koinuma, Science **291**, 854 (2001)
5. S.A. Ahmed, J. Mater. Sci.: Mater. Electron. **27**, 7589 (2016)
6. R. Janisch, P. Gopal, N.A. Spaldin, J. Phys. Cond. Matter **17**, R657 (2005)
7. D.J. Keavney, D.B. Buchholz, Q. Ma, R.P.H. Chang, Appl. Phys. Lett. **91**, 012501 (2007)
8. D. Chakraborti, G.R. Trichy, J.T. Prater, J. Narayan, J. Phys. D Appl. Phys. **40**, 7606 (2007)
9. L.H. Ye, A.J. Freeman, B. Delley, Phys. Rev. B **73**, 033203 (2006)
10. Z.A. Khan, A. Rai, S.R. Barman, S. Ghosh, Appl. Phys. Lett. **102**, 022105 (2013)
11. T.S. Herng, S.P. Lau, S.F. Yu, H.Y. Yang, X.H. Ji, J.S. Chen, N. Yasui, H. Inaba, J. Appl. Phys. **99**, 086101 (2006)
12. T.S. Herng, S.P. Lau, S.F. Yu, J.S. Chen, K.S. Teng, J. Magn. Magn. Mater. **315**, 107 (2007)
13. H. Zhu, J. Iqbal, H. Xu, D. Yu, J. Chem. Phys. **129**, 124713 (2008)
14. T. Liu, H. Xu, W.S. Chin, P. Yang, Z. Yong, A.T.S. Wee, J. Phys. Chem. C **112**, 13410 (2008)
15. S.A. Ahmed, Cryst. Res. Technol. **44**, 971 (2009)
16. H.L. Liu, J.H. Yang, Z. Hua, Y.J. Zhang, Y. Liu, J. Cao, L.H. Fei, X. Cheng, J. Mater. Sci.: Mater. Electron. **23**, 832 (2012)
17. M.S. Park, B.I. Min, Phys. Rev. B **68**, 224436 (2003)
18. T.M. Hammad, J.K. Salem, R.G. Harrison, R. Hempelmann, N.K. Hejazy, J. Mater. Sci.: Mater. Electron. **24**, 2846 (2013)
19. A. Aravind, M.K. Jayaraj, M. Kumar, R. Chandra, J. Mater. Sci.: Mater. Electron. **24**, 106 (2013)
20. P.K. Sharma, P.K. Dutta, A.C. Pandey, J. Magn. Magn. Mater. **321**, 4001 (2009)
21. H. Zhang, Z. Wen, X.O. Qi, L.A. Si, L.U. Xu, W. Zhong, D. Wu, K. Shen, M.X. Xu, T. Qiu, Q.Y. Xu, J. Alloy. Compd. **536**, 184 (2012)
22. B. Choudhury, A. Choudhury, J. Appl. Phys. **114**, 203906 (2013)
23. H.L. Liu, J.H. Yang, Y.J. Zhang, Y.X. Wang, M.B. Wei, D.D. Wang, L.Y. Zhao, J.H. Lang, M. Gao, J. Mater. Sci.: Mater. Electron. **20**, 628 (2009)
24. C. Xu, K. Yang, L. Huang, H. Wang, J. Chem. Phys. **130**, 124711 (2009)
25. A. Sundaresan, R. Bhargavi, N. Rangarajan, U. Siddesh, C.N.R. Rao, Phys. Rev. B **74**, 161306(R) (2006)
26. R. Elilarassi, G. Chandrasekaran, J. Mater. Sci.: Mater. Electron. **21**, 1168 (2010)
27. O. Perales-Perez, A. Parra-Palomino, R. Singhal, P.M. Voyles, Y. Zhu, W. Jia, M.S. Tomar, Nanotechnology **18**, 315606 (2007)
28. R. Mohan, K. Krishnamoorthy, S.-J. Kim, Solid State Commun. **152**, 375 (2012)
29. A.J. Reddy, M.K. Kokila, H. Nagabhushana, R.P.S. Chakradhar, C. Shivakumara, J.L. Rao, B.M. Nagabhushana, J. Alloy. Compd. **509**, 5349 (2011)
30. J. Wu, T.T. Li, T. Qi, B.L. Zhu, W.J. Wang, D. Wei, C.S. Xie, J. Mater. Sci.: Mater. Electron. **27**, 163 (2016)
31. J.A. Mary, J.J. Vijaya, J.H. Dai, M. Bououdina, L.J. Kennedy, Y. Song, Mater. Sci. Semicond. Process. **34**, 27 (2015)
32. J.A. Mary, J.J. Vijaya, M. Bououdina, L.J. Kennedy, J.H. Dai, Y. Song, Phys. B **456**, 344 (2015)
33. J.F. Cordaro, Y. Shim, J.E. May, J. Appl. Phys. **60**, 4186 (1986)
34. B.J. Jin, S. Im, S.Y. Lee, Thin Solid Films **366**, 107 (2000)
35. R. Wu, Y. Yang, S. Cong, Z. Wu, C. Xie, H. Usui, K. Kawaguchi, N. Koshizaki, Chem. Phys. Lett. **406**, 457 (2005)
36. A.K. Srivastava, M. Deepa, N. Bahadur, M.S. Goyat, Mater. Chem. Phys. **114**, 194 (2009)
37. S. Kumar, S. Mukherjee, R. Kr, S. Singh, A.K.Ghosh. Chatterjee, J. Appl. Phys. **110**, 103508 (2011)
38. M. Ghosh, A.K. Raychaudhuri, Nanotechnology **19**, 445704 (2008)
39. C.G. Van de Walle, Phys. B **308–310**, 899 (2001)
40. Z.-M. Liao, H.-Z. Zhang, Y.-B. Zhou, J. Xu, J.-M. Zhang, D.-P. Yu, Phys. Lett. A **372**, 4505 (2008)
41. H.B. Liu, Y. Liu, L.L. Yang, Z.G. Chen, H.L. Liu, W.J. Li, J.H. Yang, Z.P. Zhou, J. Mater. Sci.: Mater. Electron. **26**, 2466 (2015)
42. J.D. Ye, S.L. Gu, F. Qin, S.M. Zhu, S.M. Liu, X. Zhou, W. Liu, L.Q. Hu, R. Zhang, Y. Shi, Y.D. Zheng, Appl. Phys. A **81**, 759 (2005)
43. F. Leiter, H. Alves, D. Pfisterer, N.G. Romanov, D.M. Hofmann, B.K. Meyer, Phys. B **340–342**, 201 (2003)
44. V. Pazhanivelu, A.P.B. Selvadurai, R. Murugaraj, I.P. Muthuselvam, F.C. Chou, J. Mater. Sci.: Mater. Electron. **27**, 8580 (2016)
45. F. Oba, S.R. Nishitani, S. Isotani, H. Adachi, I. Tanaka, J. Appl. Phys. **90**, 824 (2001)
46. S. Lany, A. Zunger, Phys. Rev. Lett. **98**, 45501 (2007)
47. M.D. McCluskey, S.J. Jokela, J. Appl. Phys. **106**, 071101 (2009)
48. A.K. Mishra, S.K. Chaudhuri, S. Mukherjee, A. Priyam, A. Saha, D. Das, J. Appl. Phys. **102**, 103514 (2007)
49. D. Sanyal, T.K. Roy, M. Chakrabarti, S. Dechoudhury, D. Bhowmick, A. Chakrabarti, J. Phys. Cond. Matter. **20**, 45217 (2008)
50. S. Dutta, M. Chakrabarti, S. Chattopadhyay, D. Sanyal, A. Sarkar, D. Jana, J. Appl. Phys. **98**, 53513 (2005)
51. X.J. Liu, C. Song, F. Zeng, X.B. Wang, F. Pan, J. Phys. D Appl. Phys. **40**, 1608 (2007)
52. C.-H. Chien, S.H. Chiou, G.Y. Gao, Y.-D. Yao, J. Magn. Magn. Mater. **282**, 275 (2004)
53. M. Weissmann, L.A. Errico, Phys. B **398**, 179 (2007)
54. M. Wei, N. Braddon, D. Zhi, P.A. Midgley, S.K. Chen, M.G. Blamire, J.L. MacManus-Driscoll, Appl. Phys. Lett. **86**, 72514 (2005)
55. J.M.D. Coey, M. Venkatesan, C.B. Fitzgerald, Nature Mater. **4**, 173 (2005)
56. H.L. Liu, L.H. Fei, H.B. Liu, J.H. Yang, X. Jin, M. Gao, Y. Liu, X. Cheng, X. Zhang, J. Mater. Sci.: Mater. Electron. **24**, 58 (2013)